

Optimization of optode arrangements for diffuse optical tomography: A singular-value analysis

J. P. Culver,* V. Ntziachristos,* M. J. Holboke, and A. G. Yodh

Departments of Physics and Astronomy, University of Pennsylvania, Philadelphia, Pennsylvania 19104

Received August 17, 2000

We develop a method to optimize the resolution of diffuse optical tomographic instruments. Singular-value analysis of the tomographic weight matrix associated with specific data types, geometries, and optode arrangements is shown to provide a measure of image resolution. We achieve optimization of device configuration by monitoring the resolution measure described. We introduce this idea and demonstrate its utility by optimizing the spatial sampling interval and field-of-view parameters in the parallel-plane transmission geometry employed for diffuse optical breast imaging. We also compare resolution in transmission and remission geometries. © 2001 Optical Society of America

OCIS codes: 170.5280, 170.3010, 170.6510, 170.6960.

Diffuse optical tomography (DOT) is an exciting biomedical imaging modality that is currently employed by several groups of scientists focusing on clinical research.^{1–5} The rapid proliferation of diffuse optical instrumentation and image-reconstruction techniques, however, has created a need for comprehensive and objective methods to optimize and characterize DOT systems. Optimization is made difficult by the wide variety of DOT devices.^{6–9} Most generally, these devices utilize different measurement modes (time-domain, frequency-domain, continuous-wave), measurement geometries, sampling densities, regularization methods, and inversion techniques and have different signal-to-noise levels. In this Letter we show how numerical singular-value analysis of the linearized DOT forward solution provides an explicit relation among signal, noise, regularization, and resolution for DOT systems. We employ the method to optimize optode arrangements in the parallel-plane and remission geometries.

The fundamental assumption underlying our analysis is that propagation of light through tissue can be modeled by a weight matrix that maps the optical properties of tissue onto the measurements.¹⁰ The weight matrix depends on the forward model used for light transport and on device specifics such as measurement type and source-detector geometry. We examine the weight matrix by using singular value analysis^{10,11} and show how image signal and measurement noise are related to resolution through a regularization parameter. One achieves optimization of experimental parameters by monitoring the resolution measure as a function of device configuration. To demonstrate the technique we examine the affects of spatial sampling interval and field of view (FOV) in the parallel-plane geometry. The FOV informs the placement of optodes, and the sampling interval provides a cost-benefit analysis of the number of useful optodes.

For concreteness we consider the planar transmission geometry depicted in Fig. 1 wherein a one-dimensional (1D) array of sources on the input side of the sample illuminates a tissue volume and a 1D array of detectors on the output side records scattered photon density. This two-dimensional (2D) arrangement of optodes is typical of DOT systems.^{9,12} We adopt the

diffusion model for propagation of light in tissues. In addition, for expositional simplicity we limit our samples to those that contain only absorption heterogeneities and limit our description to scattered diffuse photon density waves within the linear Rytov approximation.¹² Stable inversion of such integral solutions is well established.^{10,12–14} The scattered field, Φ_i^s , is $\Phi^s(r_s, r_d)_i = \sum_{j=1}^N W_{ij} \delta\mu_{aj}$ or $\Phi^s = \mathbf{W} \delta\mu_a$. $\Phi^s(r_s, r_d)_i$ is the scattered photon density measured at detector location r_{di} due to illumination from a source located at r_{si} . $\delta\mu_a(r_j)$ represents the deviation of the sample absorption at position r_j from the sample average. \mathbf{W} is the weight matrix that characterizes diffuse light propagation from each source to each sample volume element and then on to each detector. In the Rytov approximation, $W_{ij} = C \times G(r_{si}, r_j)G(r_j, r_{di})/G(r_{si}, r_{di})$, C is a conversion factor, and $G(r, r')$ is the Green's function of the diffusion equation for the chosen sample geometry.¹² In vector notation, Φ^s is a vector with M elements (where M is the number of measurements), $\Phi^s(r_s, r_d)_i$, and $\delta\mu_a$ is a vector with N volume elements, $\delta\mu_{aj}$. \mathbf{W} is an $M \times N$ matrix with elements W_{ij} .

Singular-value decomposition of the weight matrix yields a triplet of matrices: $W_{ij} = \sum_{k=0}^{\text{rank}(W)} u_{ik} s_{kk} v_{kj}$ ($\mathbf{W} = \mathbf{U}\mathbf{S}\mathbf{V}^T$). Here \mathbf{U} and \mathbf{V} are orthonormal

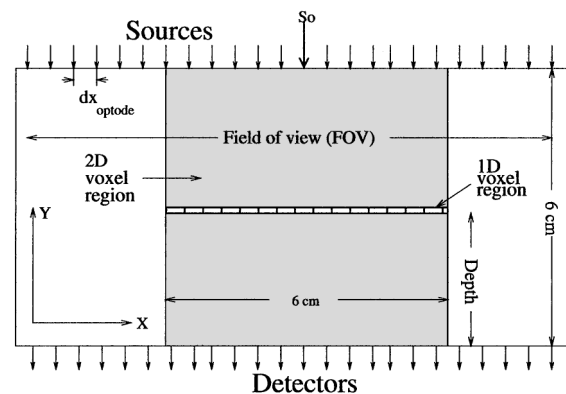


Fig. 1. Parallel plane transmission slab geometry. The optode placement sampling interval (dx_{optode}) and FOV are shown.

matrices containing the singular vectors of \mathbf{W} , and \mathbf{S} is a diagonal matrix that contains the singular values of \mathbf{W} . The vectors of \mathbf{V} correspond to image-space modes that can be used to build up any spatial distribution of absorption heterogeneity. The magnitude of the singular values of \mathbf{S} provides a measure of the relative effects of these image-space modes on the detected signal; the singular values are ordered to decrease in magnitude with increasing image-space mode indices. The vectors of \mathbf{U} correspond to detection-space modes.

To better understand the nature of singular values and vectors, consider a simple situation in which the heterogeneities are entirely contained within a 1D slice at depth d with respect to the detection surface. Furthermore, assume that the optode arrangements use equal numbers of sources and detectors, whose extent is specified by a FOV and whose separation is specified by a sampling interval (dx_{optode}). In Fig. 2(a) we illustrate the first four image-space modes (columns) of \mathbf{V} . The modes are well defined by a single effective wavelength, $\lambda_k = 2 * L/k$, where L is the linear dimension of the voxelated region and k is the column index of the singular vector. The corresponding singular-value spectra depicted in Fig. 2(b) are amplification factors that couple each image-space mode to the measurements. Notice that additional measurements affect the singular value dispersion by shifting the spectra up and (or) changing the slope of its decay.

We now develop a measure of resolution. Tikhonov regularization is a standard approach used to stabilize the image reconstruction of $\delta\mu_a$. Specifically, we minimize the following objective function¹¹: $\min(\|\mathbf{W}\delta\mu_a - \Phi^s\|_2^2 + \alpha\|\delta\mu_a\|_2^2)$ where α is the regularization parameter. The regularized inverse, $\mathbf{W}_\alpha^\#$, of \mathbf{W} is defined as $\mathbf{W}_\alpha^\# = \mathbf{V}\Theta\mathbf{S}^{-1}\mathbf{U}^T$, where Θ is a diagonal matrix containing a set of filter factors,¹¹ $f_{ii} = s_{ii}^2/(s_{ii}^2 + \alpha^2)$. Regularization reduces the affect of modes with singular values smaller than the regularization parameter (i.e., $s_{kk} < \alpha$). In practice the regularization parameter value is set by the experimental signal-to-noise ratio. For the present purpose we define signal and noise values and use the Miller criteria to set the regularization parameter. Specifically, $\alpha = \sqrt{N/M}(\|e\|_2/\|\delta\mu_a\|_2)$. By assuming that noise is white, we can define the error norm $\|e\|_2 = \sigma_0\sqrt{M}$ in terms of the noise in a single measurement, σ_0 . For the 1D heterogeneity depicted in Fig. 1 the image-space modes are characterized by an effective wavelength, $\lambda_k = 2 * L/k$. Thus a natural measure of image resolution becomes apparent. The resolution (image-space) associated with a specific regularization parameter is $\langle\text{res}\rangle \approx \lambda_{k_\alpha} = 2 * L/k_\alpha$, where k_α is the index of the singular value nearest in value to α (i.e., $S_{k_\alpha k_\alpha} \approx \alpha$).

We now draw conclusions about the spectra of Fig. 2(b). Additional measurements increase resolution because of two effects. In one case more measurements were added at the same locations, effectively increasing the measurement integration time. The singular value dispersion (i.e., the shape of the spectra) remains unchanged, but the norm of \mathbf{W} ($\|\mathbf{W}\|_2 = s_{00}$, where s_{00} is the first singular value)

changes such that $s_{00}(\text{new})/s_{00}(a) = \sqrt{M_{\text{new}}/M_a}$. However, if measurements are added at new positions (e.g., by increase of the FOV), then both the singular-value spectra magnitude and shape are modified. The spectra are again shifted up as a result of increasing measurement number. Additionally, the decay of the singular values is slower, reflecting new projection angles in the new measurements. Notice that the resolution is increased substantially by extension of the FOV.

In the process of adding more measurements, σ_0 can be kept fixed, analogous to adding a new set of detectors to be analyzed in parallel. Alternatively, σ_0 can be scaled such that σ_0/\sqrt{M} remains constant. Doing this is appropriate when one is adding serial, multiplexed sources while keeping the total data collection time constant, or, similarly, when one is using CCD camera detection and examining different pixel binning schemes.

To extend the 1D resolution measure to two and three dimensions, one must consider the dimensions of the voxelated regions with respect to the singular-value index. For a 2D voxelated region the singular-value index (k) scales as the product of the number of transverse mode oscillations times the number of longitudinal mode oscillations. The wavelengths of the transverse and the longitudinal modes scale as $\approx 1/\sqrt{k}$. For a square voxelated region with dimensions $L \times L$, the resolution measure scales as $\approx 2L/\sqrt{k_\alpha}$. Similarly for a cubic voxelated region with dimensions $L \times L \times L$ the resolution measure scales as $\approx 2L/\sqrt[3]{k_\alpha}$.

We used the 2D formulation of average resolution ($\langle\text{res}\rangle \approx 2 * L/\sqrt{k_\alpha}$) to evaluate slab geometry measurement configurations.¹⁵ To study the sampling interval, we fixed the FOV at 9 cm; then, using equal numbers of sources and detectors, we varied the interoptode spacing from 3 to 32 mm. A weight matrix was generated for each configuration. The target volume was the 6 cm \times 6 cm \times 2 mm

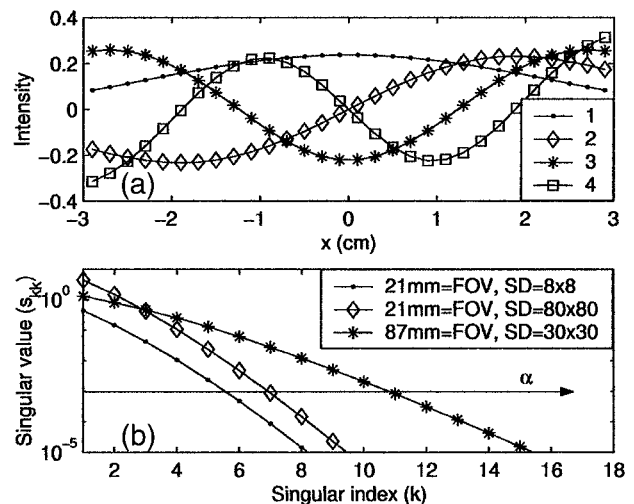


Fig. 2. (a) First four image space modes (columns of \mathbf{V}) for the 1D voxel region in Fig. 1: FOV, 87 mm; $dx_{\text{optode}} = 3$ mm; $N = 900$. (b) Singular-value spectra for $(-\bullet-)$ $N_{\text{sources}} = 8$, $N_{\text{detector}} = 8$, FOV, 21 mm; $(-\diamond-)$ $N_{\text{sources}} = 80$, $N_{\text{detector}} = 80$, FOV, 21 mm; $(*)$ $N_{\text{sources}} = 30$, $N_{\text{detector}} = 30$, FOV, 87 mm.

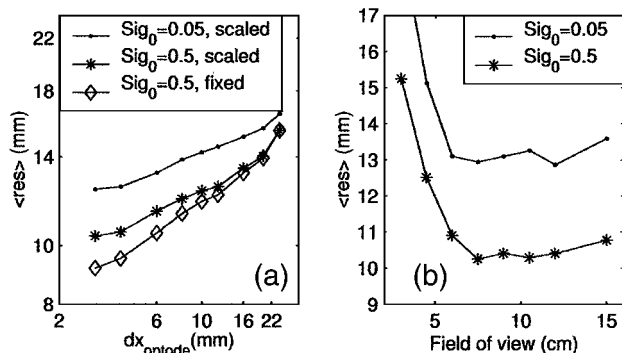


Fig. 3. (a) Resolution versus sampling interval. (b) Resolution versus field of view.

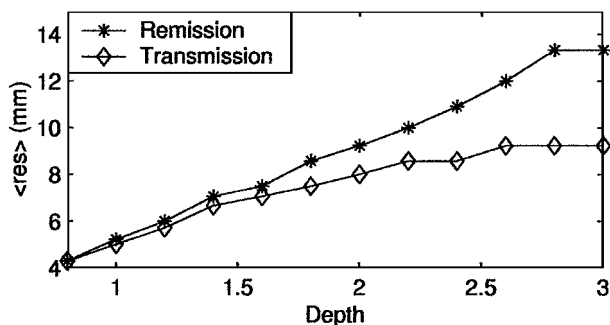


Fig. 4. Comparison of parallel-plane transmission and remission measurement geometries. For both situations, 30 detectors and 30 sources were distributed evenly over a 9-cm FOV with $\sigma_0 = 0.001$ and $\delta\mu_a * \text{vol} = 0.5$.

region depicted in Fig. 1 with 2-mm³ voxels. The effective resolution was analyzed [Fig. 3(a)] for both scaled-per-measurement noise ($\sigma_0/\sqrt{M} = 0.0003$) and constant-per-measurement noise ($\sigma_0 = 0.01$) and for two different signal levels ($\text{Sig}_0 = \delta\mu_a * \text{vol}$). The resolution was found to improve with decreasing sample interval for σ_0 held fixed. When σ_0/\sqrt{M} was held constant, the resolution still improved with decreasing sampling interval, although not so dramatically for sampling intervals below 10 mm. The signal-to-noise level thus restricts the useful sampling interval. For example, at lower signal levels, resolution does not improve for sampling intervals below 6 mm; at higher signal levels, resolution continues to improve with sampling intervals down to 3 mm, although the improvement is more costly, with an ~30% improvement requiring a 300% increase in the number sources and detectors.

Next consider the optimum FOV for the same geometry. That is, given a fixed number of measurements, how should the optodes be arranged on the measurement surface? In this instance 45 detectors and 45 sources are distributed evenly over a specified FOV with $\sigma_0 = 0.01$. In Fig. 3(b) we plot resolution for FOV's of 2–16 cm. A broad range of FOV's is seen to be optimal, and the analysis instructs us to use a FOV a few centimeters larger than the largest anticipated tissue volume.

As a final example we compare remission and transmission parallel-plane geometries (Fig. 4). The

transmission geometry is as previously described, and the remission geometry switches the detectors over to same side as the sources. The transverse resolution is determined using the 1D voxelized region of Fig. 1, and $\langle \text{res} \rangle \approx 2 * L/k_a$. At shallow depths (0–1.5 cm) the resolution is found to be similar for both geometries, but for deeper tissues (1.5–3 cm) the resolution is significantly better in the slab transmission geometry. This result illustrates the increased challenge for DOT in applications such as functional brain imaging that require remission geometries.

We have presented an optimization scheme for DOT that evaluates image-reconstruction performance using a resolution measure that is sensitive to device specifics. This technique is potentially quite general. Possibly other aspects of the instrument that are explicitly included in the forward model may be optimized by this approach.

We thank B. Chance, C. Cheung, and D. Patanayak for useful discussions and gratefully acknowledge support from National Institutes of Health grant RO1-CA60182-05 and U.S. Army grant DAMD17-97-1-7272. J. P. Culver's e-mail address is jculver@nmr.mgh.harvard.edu.

*Current address, Massachusetts General Hospital, Harvard Medical School, Charlestown, Massachusetts 02129.

References

1. B. W. Pogue, S. P. Poplack, T. O. McBride, W. A. Wells, K. S. Osterman, U. L. Osteberg, and K. D. Paulsen, *Radiology* **218**, 261 (2001).
2. V. Ntziachistos, A. G. Yodh, M. Schnall, and B. Chance, *Proc. Natl. Acad. Sci. USA* **97**, 2767 (2000).
3. D. A. Benaron, S. R. Hintz, A. Villringer, D. A. Boas, A. Kleinschmidt, J. Frahm, C. Hirth, H. Obrig, J. C. van Houten, E. L. Kermit, W. F. Cheong, and D. K. Stevenson, *J. Cereb. Blood Flow Metab.* **20**, 469 (2000).
4. S. B. Colak, M. B. van der Mark, G. W. Hooft, J. H. Hoogenraad, E. W. van der Linden, and F. A. Kuijpers, *IEEE J. Sel. Top. Quantum Electron.* **5**, 1143 (1999).
5. M. A. Franceschini, K. T. Moesta, S. Fantini, and G. Gaida, *Proc. Natl. Acad. Sci. USA* **94**, 6468 (1997).
6. D. A. Boas, M. A. O'Leary, B. Chance, and A. G. Yodh, *Appl. Opt.* **36**, 75 (1997).
7. C. L. Matson and H. Liu, *J. Opt. Soc. Am. A* **16**, 455 (1999).
8. Y. L. Pei, F. B. Lin, and R. L. Barbour, *Opt. Express* **5**, 203 (1999), <http://epubs.osa.org/opticsexpress>.
9. B. W. Pogue, T. O. McBride, U. L. Ostererg, and K. D. Paulsen, *Opt. Express* **4**, 270 (1999), <http://epubs.osa.org/opticsexpress>.
10. S. R. Arridge, *Inverse Probl.* **15**, R41 (1999).
11. H. W. Engl, M. Hanke, and A. Neubauer, *Regularization of Inverse Problems* (Kluwer Academic, Dordrecht, The Netherlands, 1996), pp. 117–126.
12. M. A. O'Leary, D. A. Boas, B. Chance, and A. G. Yodh, *Opt. Lett.* **20**, 426 (1995).
13. X. D. Li, D. Pattanayak, B. Chance, and A. G. Yodh, *Opt. Lett.* **22**, 573 (1997).
14. J. C. Schotland, *J. Opt. Soc. Am. A* **14**, 275 (1997).
15. An analysis incorporating depth-dependent regularization produced similar results.